Flexible VO$_2$ Films for In-Sensor Computing with Ultraviolet Light

Ge Li, Donggang Xie, Ziye Zhang, Qingli Zhou, Hai Zhong, Hao Ni, Jiaou Wang, Er-jia Guo, Meng He, Can Wang, Guozhen Yang, Kuijuan Jin,* and Chen Ge*

With their unique advantages in portability, shape adaptability, and human friendly surfaces, flexible electronics pave the way for the implementation of wearable electronic textiles and human–machine interfaces. Although organic materials are promising for flexible devices because of the low-cost manufacturing and inherent flexibility, they meet challenges in harsh environments such as ultraviolet (UV) irradiation, which limits their applicability in UV sensors. Here, a flexible UV neuromorphic sensor is presented using inorganic vanadium dioxide (VO$_2$) films grown on mica substrates. The flexible device shows UV photoinduced nonvolatile phase transition, and can be reversibly modulated using electrolyte gating. The optical responses remain almost unchanged after 10 000 bending cycles or at small bending radius, exhibiting high tolerance to the bending deformation. Besides, the variations in image recognition accuracy under different bending conditions keep within 1.6%, indicating that the device can be adapted to various deformation conditions. By constructing near-/in-sensor computing architectures using the flexible VO$_2$ neuromorphic sensors with photoinduced nonvolatile phase transition, both static image processing and motion detection are realized without redundant and massive information transfer. This result lays the foundation for the development of flexible UV neuromorphic sensors.

1. Introduction

With their unique advantages including wearability, printability, foldability, and stretchability,[1–3] flexible electronics have attracted great attention in the past few years. They have broad application prospects in healthcare,[4] emerging display technologies,[5] human–machine interfaces,[6,7] wearable electronic textiles,[8] and flexible sensors used in the internet-of-things applications.[9,10] Currently, studies of flexible devices are dominated by organic materials due to their benefits in low-cost manufacturing, flexibility, and biological compatibility. However, these types of devices suffer from some shortcomings, such as dissolution in water or organic solvents and difficulty in the large-scale integration, which limit their further development.[11–13] More importantly, the organic materials' inherent characteristics, including long molecular chains and relatively weak covalent bonds, make them susceptible to degradation, which restricts their application in some extreme environments. For example, the high photon energy of ultraviolet (UV) light can destroy their molecular skeleton,[14] leading to organic UV sensors suffering from nonreversibility, insensitivity, and small change in current.[15–17] In specific environments, the information detection and processing of UV emissions are desirable.[18] As an alternative to organic-material-based devices, developing flexible inorganic devices is considered a feasible solution due to their good electrical properties, power efficiency, and reliability.[11,19–21] Nonetheless, the required high fabrication temperatures make them difficult to grow on flexible substrates directly, leading to a series of

G. Li, D. Xie, Z. Zhang, H. Zhong, E.-j. Guo, M. He, C. Wang, G. Yang, K. Jin, C. Ge
Beijing National Laboratory for Condensed Matter Physics
Institute of Physics
Chinese Academy of Sciences
Beijing 100190, China
E-mail: kjjin@iphy.ac.cn; gechen@iphy.ac.cn
G. Li, C. Wang, K. Jin, C. Ge
School of Physical Sciences
University of Chinese Academy of Sciences
Beijing 100049, China

D. Xie, H. Ni
College of Science
China University of Petroleum (East China)
Qingdao 266580, China
Z. Zhang, Q. Zhou
Key Laboratory of Terahertz Optoelectronics
Ministry of Education
and Beijing Advanced Innovation Center for Imaging Theory and Technology
Department of Physics
Capital Normal University
Beijing 100048, China
J. Wang
Beijing Synchrotron Radiation Facility
Institute of High Energy Physics
Chinese Academy of Sciences
Beijing 100049, China

process-related issues. As a result, the implementation of flexible inorganic devices still faces significant challenges.[11]

Among various materials used for inorganic flexible devices, the VO$_2$/mica heterostructure offers several advantages. The mica substrate has high temperature tolerance; so, the film can be directly grown on it via van der Waals (vdW) epitaxy.[22] In addition, its atomic-level peeling characteristic allows devices to be converted from rigid to flexible through a reduction of the substrate thickness to less than 100 nm using mechanical exfoliation.[23,24] Hence, flexible devices using mica substrates have good flexibility while avoiding a series of issues, like performance degradation due to difficulties in fabrication processing.[11] As an archetypal Mott material, vanadium dioxide (VO$_2$) has a first-order metal–insulator transition above room temperature.[25–28] It has outstanding characteristics including fast switching speeds, high reliability, excellent nonvolatility, and scalability as good as other phase-change materials.[29,30] Compared to other phase-change materials, VO$_2$ has a variety of existing phases,[31,32] whose formation energies are similar. Thus, transformation between these existing phases can be readily realized by external field excitations. Several works have shown that high-quality VO$_2$ films can be epitaxially grown on the flexible mica substrates, and the change of resistance can reach three orders of magnitude.[22,33,34] In addition, VO$_2$ has a photoinduced nonvolatile phase transition under UV irradiation,[35] and its optical response can reach to sub-picosecond scale.[36–38] These characteristics make the VO$_2$/mica heterostructure ideal for flexible devices aimed at UV information sensing and processing. Therefore, a high-quality VO$_2$/mica heterostructure may provide new options for the construction of flexible optoelectronic sensors with good stability and reliability.

With the rapid development of flexible optoelectronics in recent years, requirements have increased for strong data-processing capabilities, low power consumption, and robust bending stability.[39] Neuromorphic sensors that integrate sensing, memory, and processing functions together can greatly reduce high power consumption caused by physical separation of each functional component in conventional artificial intelligence systems.[40,41] Through moving the computation tasks to the sensory terminals, we can eliminate the data transfer within in-sensor computing architecture consisting of neuromorphic sensors, and then greatly shorten the latency. Recently, several flexible UV sensors, which integrated sensing and memory functions, have been investigated.[42–44] However, these devices still have considerable margins for improvement of some performance aspects, such as retention and bending tolerance.[45,46] Besides, these works on flexible neuromorphic UV sensors are limited to static image processing, while the extraction and detection of motion targets based on neuromorphic sensors remain unexplored.

In this work, we present a prototype neuromorphic UV sensor with good flexibility and bending stability based on a VO$_2$/mica heterostructure. The photoinduced nonvolatile phase transition of VO$_2$ films bestows the neuromorphic sensors with good multilevel storage and retention characteristics. The nonvolatile phase transition can be reversibly regulated using electrolyte gating. The proposed UV neuromorphic sensors exhibit high tolerance to bending deformation, and the optical response remains almost unchanged even after 10 000 bending cycles or at a 3 mm bending radius. Moreover, we construct an artificial neural network (ANN) to realize static image processing. The image recognition rate on the Modified National Institute of Standards and Technology (MNIST) handwritten database reaches 93%, and the variation range under different bending conditions is only 1.6%, which is similar to the error caused by the neural network itself during the training process. Motion detection and recognition are also demonstrated through an in-sensor computing architecture consisting of the proposed devices.

2. Results and Discussion

2.1. Photoinduced Nonvolatile Phase Transition in Flexible VO$_2$ Films

High-quality vdW epitaxial VO$_2$ films were deposited on mica substrates through pulsed laser deposition (PLD) technique. More details on the film growth process are given in the "Experimental Section." The high-resolution reciprocal spatial mapping (RSM) was used to confirm the crystalline quality of the VO$_2$/mica heterostructure and its epitaxial relationship (**Figure 1**a). The result reveals that, in addition to mica (003) and (004) peaks, the film presents only a VO$_2$ (020) peak without any impurity phase or other crystal orientations. The epitaxial relationships consistent with previous reports are determined as VO$_2$ (010) ∥ mica (001); VO$_2$ (100), (001), and (101) ∥ mica (100); and VO$_2$ (10$\bar{2}$), (20$\bar{1}$), and (101) ∥ mica (010).[34,47] This result indicates that the VO$_2$ film is strain free. We first investigated the effect of the illumination wavelength on the flexible VO$_2$ film. As shown in Figure S1 (Supporting Information), the film exhibits a significant nonvolatile modulation only under UV exposure, while no memory effect is observed in visible wavelengths. To further study the mechanism behind the nonvolatile modulation under UV irradiation, we carried out characterization measurements for a series of VO$_2$ films irradiated with various UV exposure durations.

Figure 1b shows temperature-dependent resistance (R–T) curves in VO$_2$ films. The light intensity was fixed at 3.5 W cm^{-2}. The film without UV illumination exhibited typical thermal hysteresis with a resistance change by three orders of magnitude. The thermal hysteresis may be ascribed to the lattice incompatibility between transformed and parent phases.[48] As the exposure duration increased, the insulator–metal phase transition was gradually suppressed, and the resistance stabilized in the metallic state even below the transition temperature after 42 h irradiation. The giant nonvolatile modulation of VO$_2$ under strong light intensity is helpful to study the underlying mechanism during the photoinduced phase transition. Accompanied with the change in resistance, a pronounced optical switching in the infrared region was also observed during the phase-transition process (Figure 1c). In the initial state, the VO$_2$ film performed high transmittance in the infrared band and reached a peak of 63% at 2250 nm at room temperature, while it decreased significantly under UV irradiation. The transmittance reduced to a minimum value of 12% after 42 h of illumination. Since the infrared spectrum of VO$_2$ is sensitive to
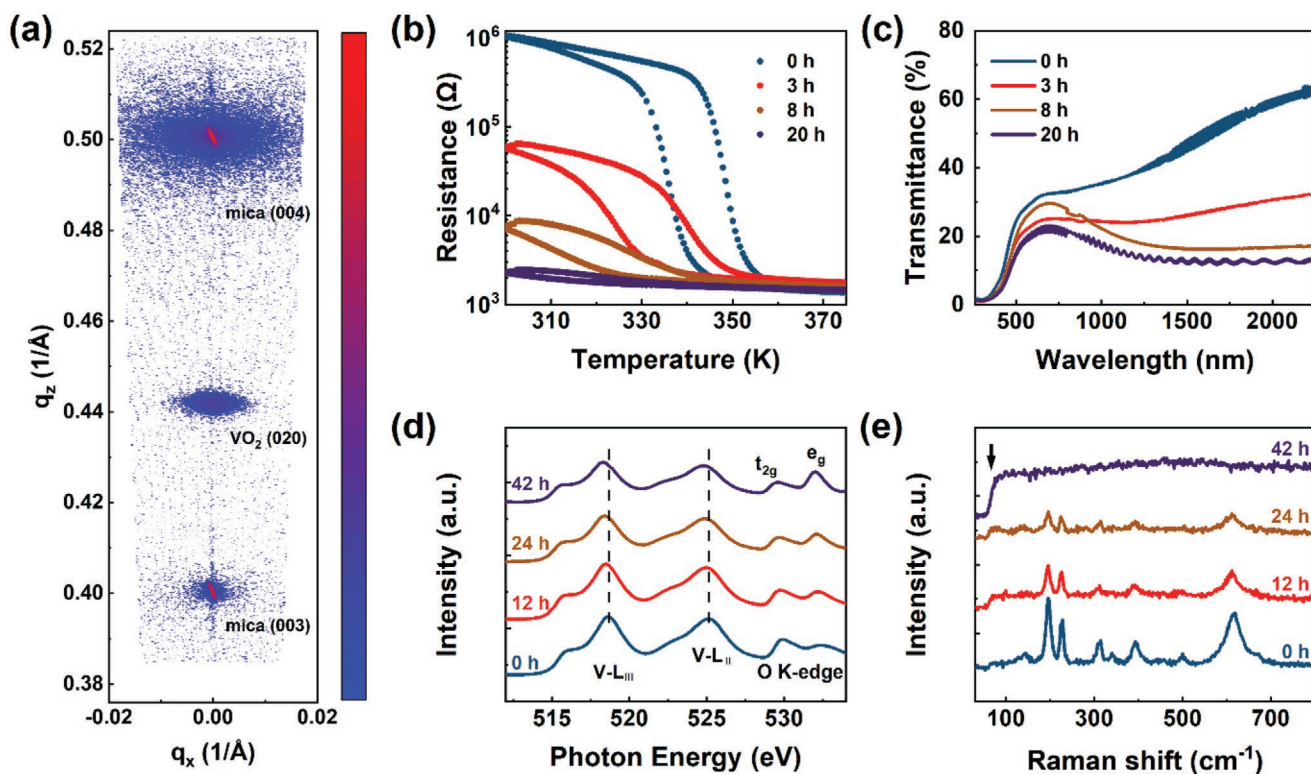
Figure 1. High-quality VO_2/mica film and photoinduced nonvolatile phase transition. a) RSM of VO_2 film grown on the mica substrate. b) Temperature-dependent resistance curves. c) Transmittance spectra at room temperature, d) V L-edge and O K-edge XAS curves and e) Raman spectra in VO_2 film under 3.5 W cm^{-2} UV irradiation for different times.

the density of carriers, that is, the absorption and reflection increased with the increasing of carrier concentration, the dramatic decrease of the transmittance also indicated the transition in electrical properties of VO_2 film. The evolution of electronic structure during the UV irradiation process was further investigated using the X-ray absorption spectrum (XAS) (Figure 1d). The $V–L$ peaks shifted toward the low photon energy direction with increasing the exposure duration, reflecting that the V^{4+} transformed toward a lower valence state. Besides, the value of t_{2g}/e_g at the O K-edge spectrum decreased significantly due to the gradually filled of $d_{//}$ and π^* orbitals by electrons. The decrease of t_{2g} intensity in O K-edge can be attributed to the increase of oxygen vacancies,[49] which may be induced by UV irradiation.

Raman spectroscopy was employed to explore the change in the lattice structure (Figure 1e). The as-grown VO_2 film exhibited a typical monoclinic structure belonging to the $P2_1/c$ space group (M_1 phase).[50–53] Raman peaks locate at 146, 196 (A_g), 228 (A_g), 261 (B_g), 314 (A_g), 340 (A_g), 393 (A_g), 443 (B_g), 500 (B_g), 618 (A_g), and 673 cm^{-1} (B_g). As the UV illumination duration increased, the strength of M_1 phonon mode was gradually reduced, and finally transformed to a featureless luminescence. The rise of luminescence background (the position pointed by the arrow) reflects the formation of metallic rutile domains.[50,54] The X-ray diffraction (XRD) patterns further confirm that the structural phase transition existed during the UV modulation process (Figure S2, Supporting Information). The VO_2 peak shifted to the low-angle region, revealing the transi-

tion from $(020)_M$ to $(200)_R$ family peaks.[55] The transformation can be attributed to the effect of oxygen vacancies. The calculation result showed that the vacancy formation energy is about 3.33 eV when removing one oxygen atom at the surface of the slab in VO_2 films.[56] This value can be reduced to 2.9 eV by strain engineering.[57] UV light with photon energy higher than this value can produce oxygen vacancies, leading to nonvolatile phase transition, while visible light with lower photon energy can only achieve volatile modulation.

2.2. Flexible Sensors with Optoelectronic Transistor Structure

A large-scale VO_2 film (40 mm × 40 mm) was grown and fabricated into a flexible optoelectronic transistor array (**Figure 2**a). The schematic of a single device is shown in Figure S3a (Supporting Information). We adopted a droplet ionic liquid as the dielectric layer, which covered both the VO_2 channel and the gate-terminal electrode. There are many inorganic solid-state electrolytes such as porous silica[58] and GdO_x,[59,60] which can achieve the same gating effect. The devices exhibited Ohmic contact between source and drain electrodes (Figure S3b, Supporting Information). More fabrication details are given in the "Experimental Section." The transfer curve (Figure S4, Supporting Information) exhibits a typical hysteresis loop by sweeping V_G from 2.5 to −3 V. This result indicates that the channel current could be reversibly switched between low and high nonvolatile states.[61] We randomly selected 100 devices to
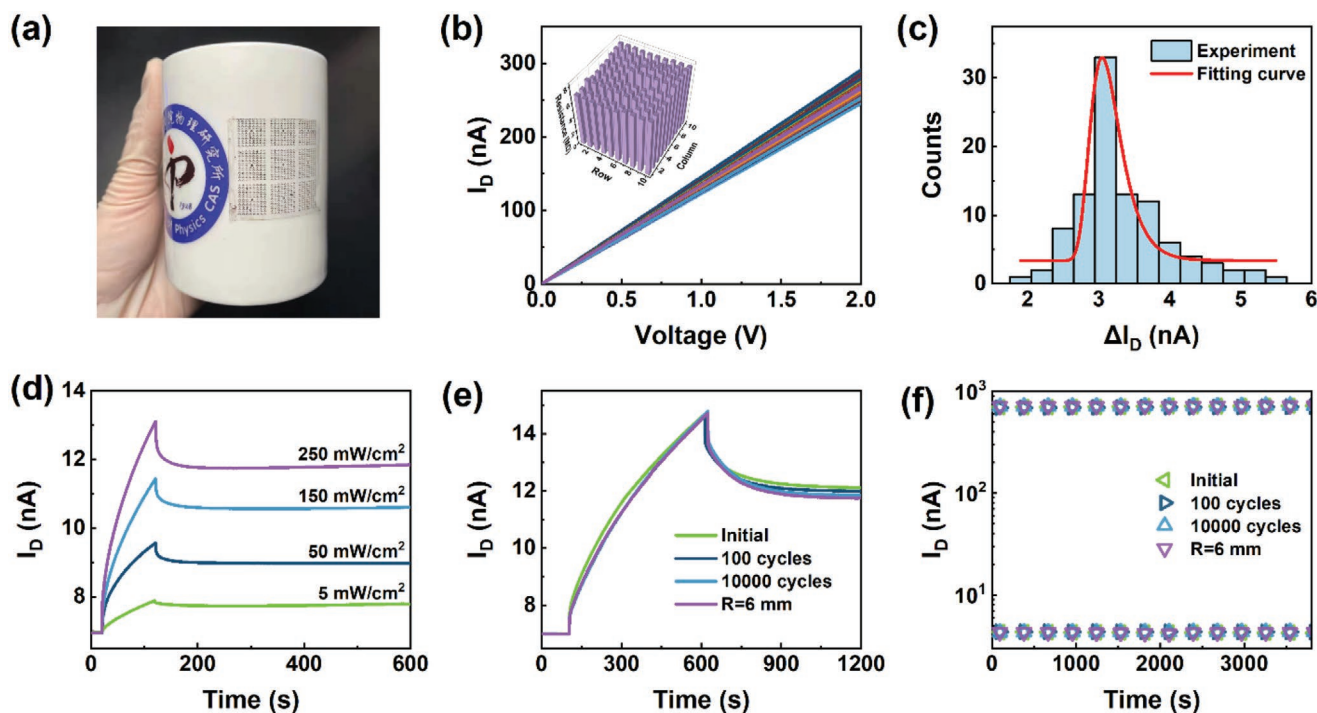
Figure 2. Device performance on flexible mica substrates. a) A photograph of a 3×3 device array on a 40 mm $\times$ 40 mm mica substrate. b) $I–V$ curves of 100 devices randomly selected from the device array (inset: resistance histogram of the devices). c) Statistical diagram of current variation of selected devices after UV irradiation (150 mW cm^{-2} for 100 s). The fitting curve is a Gaussian function. d) Intensity-dependent plasticity under 100 s UV irradiation. e) I_D as a function of time after 500 s of UV exposure under 300 mW cm^{-2}. f) Retention characteristics after 2 h exposure under 1 W cm^{-2} at different bending conditions. During the measurements, bending radius is 6 mm, and bending cycles are 100 and 10 000 times.

examine the device-to-device variation (Figure 2b). $I–V$ curve distribution of the devices is relatively concentrated, reflecting uniformity of flexible VO$_2$ film. The statistical distribution histogram of the optical response shows that after exposure to UV light (150 mW cm^{-2} for 100 s), 76% of the devices have a nonvolatile current change greater than 3 nA (Figure 2c). Since the device states can be programmed by UV illumination, the basic features of synaptic plasticity were simulated to emulate learning and memory functions. Nonvolatile modulation and good stability of the channel current (I_D) were observed after 100 s of UV irradiation under different light intensities with a monitored voltage of 50 mV (Figure 2d). Figure S5 (Supporting Information) shows that the nonvolatile current change can also be programmed by increasing the illumination duration. Moreover, nonvolatile multilevel conductance states can be realized by varying the pulse number and pulse width (Figure S6, Supporting Information). To further confirm this behavior, we stimulated the device using a series of UV light pulses with a fixed light intensity and pulse width (Figure S7, Supporting Information). It was found that the nonvolatile current change linearly depends on the UV dose. UV dose can be calculated by the following equation: UV dose (mJ cm^{-2}) = UV intensity (mW cm^{-2}) $\times$ Exposure time (s). During the reset process, electrolyte gating was utilized to make the device return to its initial state by inserting oxygen ions to the irradiated VO$_{2-\delta}$ films.[62] Particularly, the large electric double-layer capacitance generated during the electrolyte gating process can lower the applied gating voltage, and thereby reduce energy consumption.[61,63] Then, we combined UV irradiation and electrolyte

gating to achieve reversible nonvolatile multilevel control of VO$_2$ films. Under UV irradiation, oxygen could be capable of releasing from the VO$_2$ film due to its low activation energy,[35] thus leading a transition from insulator monoclinic phase to metallic rutile phase. Electrolyte gating with negative V_G could insert O^{2-} into VO$_2$ through hydrolysis reaction[62] and drive the VO$_2$ film to its initial state. Therefore, reversible nonvolatile phase transformation can be achieved through the extraction/injection of the O^{2-}. The reversible modulation of optical writing and electrical erasing indicated good stability at each state, and the channel current remained constant for at least 3600 s (Figure S8, Supporting Information).

Then, we investigated the flexibility and mechanical stability by testing the optical response under different bending radii and after different bending cycles, respectively. Here, the calculation equation for bending radii is given in Note S1 (Supporting Information). Figure 2e shows similar relaxation time and nonvolatile current change after the removal of UV light under various bending states, indicating that the device still has a photoinduced nonvolatile phase transition in the bent state. We measured the device under a bending radius of 6 mm, and 100/10 000 times bending cycles. The retention characteristics at different bending conditions were measured after a 2 h UV exposure with an intensity of 1 W cm^{-2} (Figure 2f). The result indicated that I_D changed more than two orders of magnitude to a high-current state after UV irradiation, while the switching ratios and retention characteristics at different bent states maintain nearly consistent with those at the flat state. The photoinduced phase transition of VO$_2$ is marginally

**ADVANCED
SCIENCE NEWS**

www.advancedsciencenews.com

**ADVANCED
FUNCTIONAL
MATERIALS**

www.afm-journal.de

affected by its bending deformation, which lays the foundation for the realization of wearable and flexible electronic devices. Compared with the previous work, the flexible VO_2 device has good reversible regulation in synaptic function and mechanical stability (Table S1, Supporting Information).

2.3. Bending Tolerance of Device

We further studied the temperature dependence of resistance in flexible VO_2 films under various bending conditions (**Figure 3**a,b). A photograph of this bending equipment is shown in the inset of Figure 3a. During the measurements, the flexible VO_2 heterostructure was fixed on the copper bar and could be bent to any states. The measurement under bending deformation was performed with bending radii of 7, 4, and 3 mm, respectively. We examined bending cyclability for 50, 150, and 500 times with a bending radius of 6 mm, respectively. The R–T curves of VO_2 film exhibited no significant variation under different bending radii and after different bending cycles compared with that in a flat state. It proved that the electronic structure of VO_2 preset negligible change during the bending process. We measured the morphological evolution of the VO_2 films under different exposure times and bending cycles using an atomic force microscope (AFM), as shown in Figure S9 (Supporting Information). It can be seen that the UV irradiation shows almost no effect on the surface morphological evolution of the VO_2 films, while bending deformation makes the film surface slightly rough. In addition, we utilized the Raman spectrum to investigate the effect of bending states on the lattice
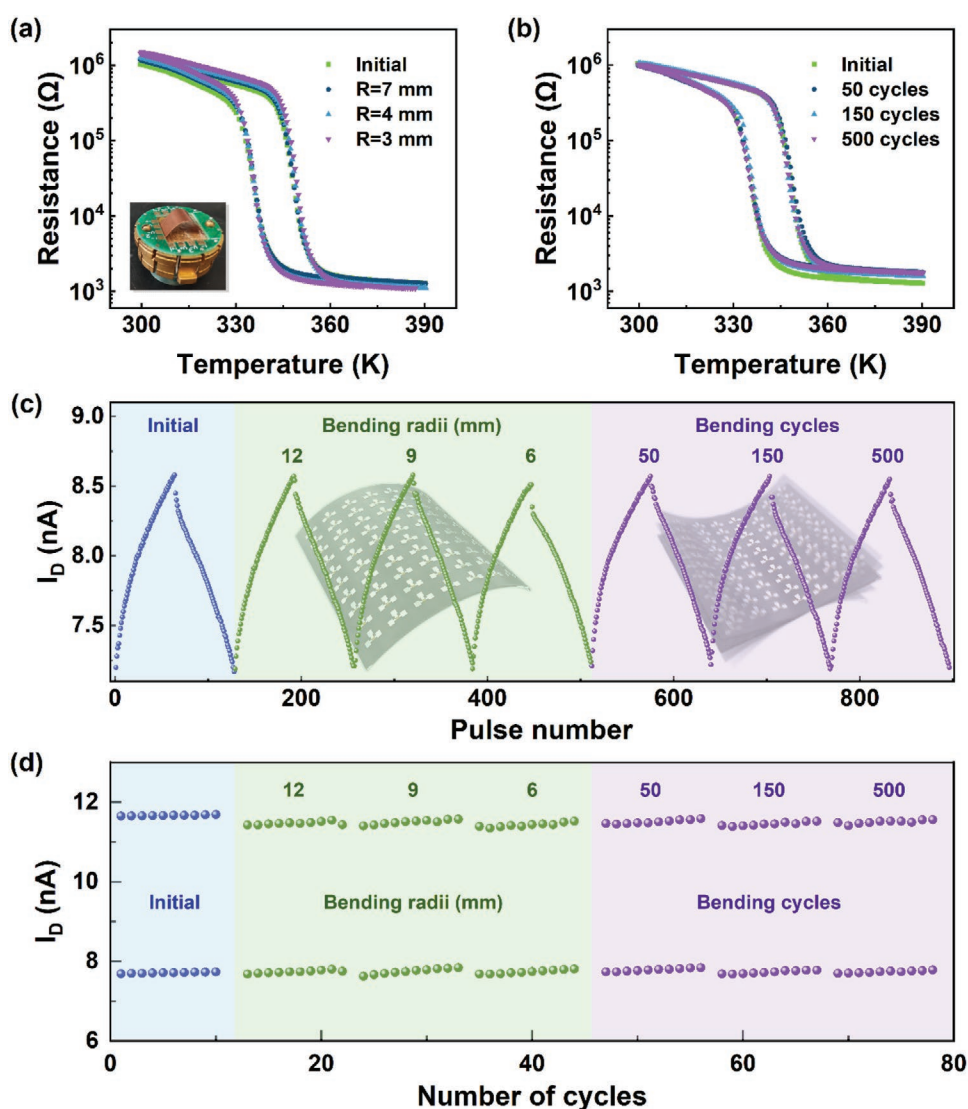

Figure 3. Mechanical flexibility. Temperature-dependent resistance curves of VO_2 film under a) different bending radii (7, 4, 3 mm, respectively) and b) different numbers of bending cycles (50, 150, 500, respectively). The inset is a photograph of the bending equipment. c) LTP and LTD of VO_2/mica device under initial and bent states by applying 64 optical pulses (50 mW cm^{-2} 5 s) and 64 V_G pulses (voltage ranging from −0.4 to −1.03 V, 4 s). d) Pulse-switching characteristics under different bending conditions with optical potentiation (250 mW cm^{-2} for 10 s) and electrical depression (−3 V for 10 s). The maximum and minimum points of I_D during the writing/erasing operation were extracted.

structure (Figure S10, Supporting Information). The phonon-mode frequencies of M_1 phase do not exhibit any movement, indicating that the VO_2 maintained in the insulating monoclinic phase. The robustness of VO_2 in electronic and structural properties under different bending conditions can be attributed to thin mica in thickness ≈0.01 mm due to its atomic-level peeling characteristic. Since the tensile strain can be given by the ratio of the whole sample's thickness to the bending radius,[3,64] a 3 mm bending radius only induced a strain of ≈0.17%, far less than the strain limit of the VO_2 films.[51]

To implement practical application in flexible neuromorphic sensors, it is essential to ensure stable synaptic functions under mechanical deformation conditions. We evaluated the long-term synaptic plasticity, including long-term potentiation (LTP) and long-term depression (LTD), under flat and different bending conditions (Figure 3c). We applied 64 continuous optical pulses to emulate LTP (pulse intensity of 50 mW cm^{-2} a duration of 5 s), while 64 V_G pulses (voltage varying from −0.4 to −1.03 V, a duration of 4 s) were applied to the gate electrode to emulate LTD. We optimized the linearity of LTD by adjusting the negative V_G from −0.4 to −1.03 V. The result demonstrates that our device presented continuously adjustable nonvolatile states no matter in which bending deformation. LTP/LTD behaviors in the six bending states were basically consistent with those in the flat state, confirming good bending tolerance of the device. In addition, pulse switching characteristics between the high- and low-current states under various bending conditions were measured by optical set (light intensity of 250 mW cm^{-2} a duration of 10 s) and electrical reset (voltage of −3 V, a duration of 10 s), as shown in Figure 3d. The bistable switching can be further demonstrated by extending the number of cycles to 100 times (Figure S11, Supporting Information). It is shown that the on/off states are maintained without significant degradation, and the switching characteristics performed ignor-

able variation after different bent treatment. In brief, these features indicate that our device has mechanically stable synaptic functions.

2.4. Multifunction Processing and Motion Detection

Next, we fabricated a 3 × 3 array composed by VO_2-based flexible neuromorphic devices, and tested the image perception and storage capability under different bending conditions to simulate different wearable states, as shown in **Figure 4**. The same images of letter "I" were written using 100 mW cm^{-2} UV irradiation, where each VO_2 transistor corresponding to one image pixel. The letters were recorded by measuring the change of channel current before UV stimulus, under a 500 s UV stimulus, and 300 s after UV light removal. We also tested the retention characteristic after another 300 s. Although the decrease of ΔI_D was observed after removing the light stimulus, the device array performed a nonvolatile feature to UV image for a long while. The different devices exhibited similar variation of I_D, indicating that the array had slightly device-to-device variation. Besides, the nonvolatile behavior of neuromorphic sensor array remained almost unchanged under different bending deformations.

In order to explore the applicability of the proposed devices in bioinspired neuromorphic visual system, a typical ANN was established for testing the MNIST database.[65] It is worth mentioning that the whole system had a near-sensor computing architecture, which allowed an original image with 28 × 28 pixels to be sensed and memorized by the sensor unit. Such independent nonvolatile storage of input information enables this system to easily achieve multifunction processing simultaneously, such as pattern classification and edge enhancement (**Figure 5**a). For pattern classification, the
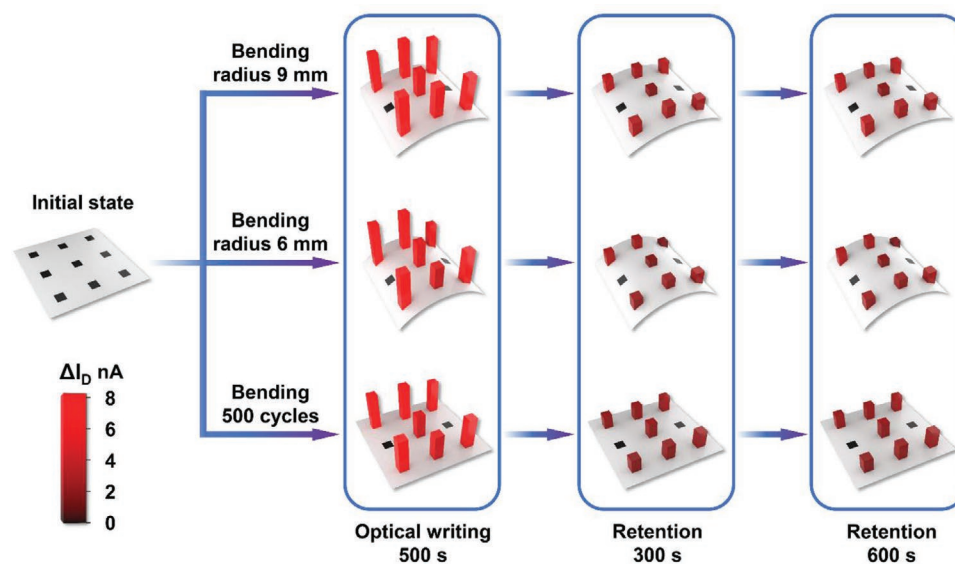

Figure 4. Image recognition and memorization of device array under various bending conditions. Under three bending states, the letter "I" was successfully written after 500 s of light exposure. The image information existed for 300 s after light removal, and this nonvolatile channel current was continuously retained with almost unchanged for 600 s. Letters were written using 100 mW cm^{-2} UV light, and the change in the original channel current signal (ΔI_D) was represented using color. The three bending states corresponded to bending radii of 9 and 6 mm, and bending numbers for 500 cycles.

**ADVANCED
SCIENCE NEWS**
www.advancedsciencenews.com

**ADVANCED
FUNCTIONAL
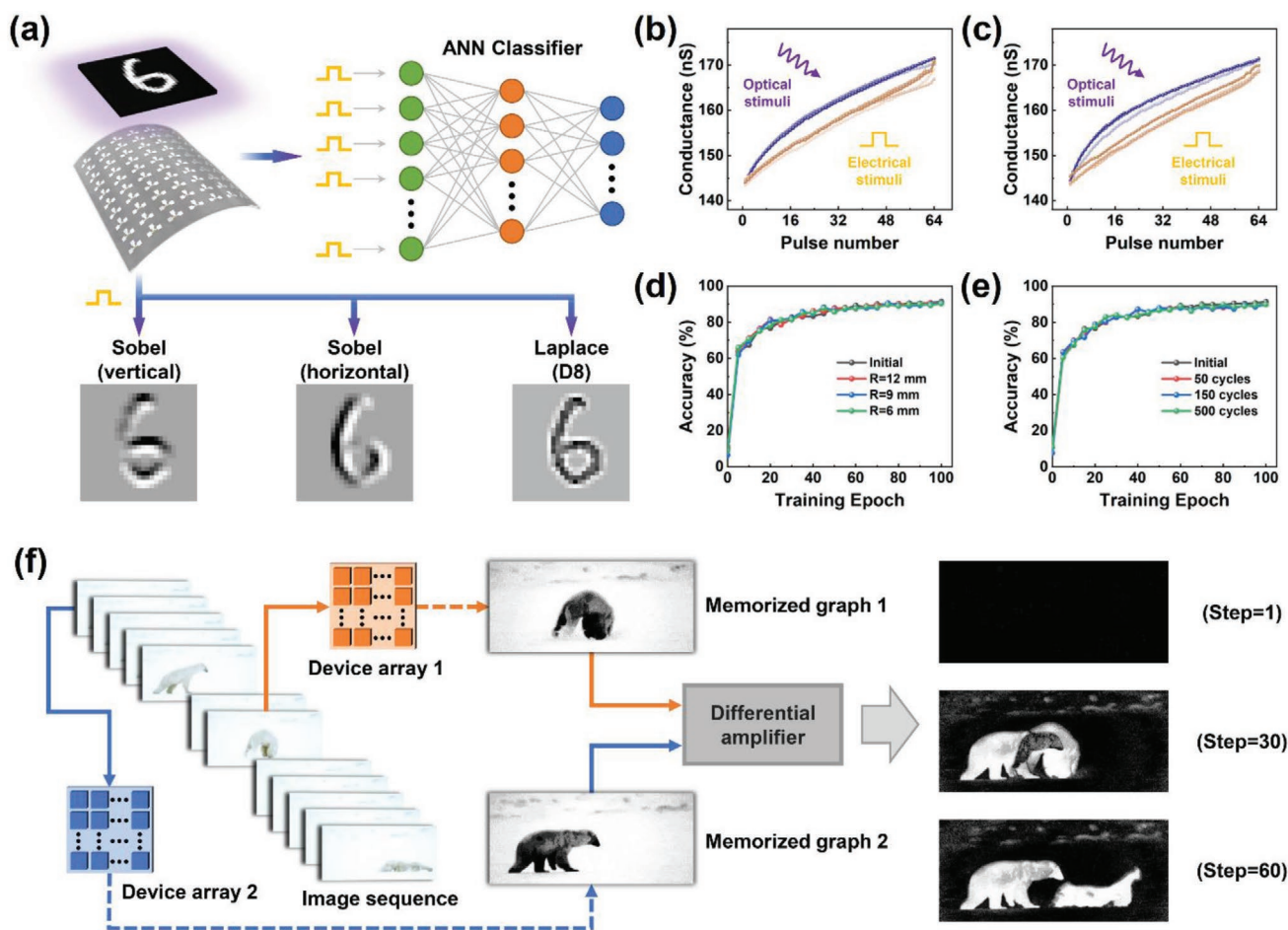MATERIALS**
www.afm-journal.de

Figure 5. Pattern recognition and motion detection. a) Schematic diagram of the near-sensor computing architecture for multitasking, including the recognition of MNIST dataset and edge-enhancement processing. Two Sobel convolution kernels were used for vertical and horizontal edge detections, respectively, and the Laplace convolution kernel was used to detect edges in all directions. Overlapping diagrams of LTP/LTD processes of the device under b) different bending radii (R=12, 9, 6 mm, respectively) and c) after different bending cycles (50, 150, 500 times). The recognition accuracy of the ANN classifier under d) different bending radii and e) after different bending cycles. f) Illustration of motion detection based on the mentioned device arrays.

image information could be read out from the sensor unit by voltage and passed to the ANN classifier, which is a two-layer fully connected network. In such an ANN classifier, the devices were used as interlayer connections between neurons, which weighted the output values of the previous layer to the next layer. The LTP and LTD properties of the synaptic devices were used to imitate the plasticity of synapses, and the training of ANN was achieved through the back-propagation algorithm.[66] In addition, the image information memorized by sensor units could also be processed simultaneously by other functional modules, such as the edge-enhancement module. The edge enhancement is an image-processing method that can highlight specific edge information while weakening other information. It is often used to identify different object types and delineate their distribution ranges. To demonstrate that, three typical convolution kernels were constructed based on the tunable nonvolatile conductance state of the device to perform edge enhancement simultaneously, which includes two Sobel convolution kernels for vertical and horizontal edge detection and one Laplace convolution kernel for edge detection in all

directions. The detailed operation processes of the ANN classifier and edge enhancement are given in Figure S12 and Note S2 (Supporting Information). To evaluate the performance of the classifier under different bending conditions, LTP/LTD and recognition accuracy were selected as performance metrics. The effects of different bending radii (12, 9, and 6 mm; Figure 5b,d) and different numbers of bending cycles (50, 150, and 500; Figure 5c,e) on device performance were investigated, respectively. Figure 5b,c shows good bending stability for the LTP/LTD processes. The recognition accuracy was also stable under bending conditions (Figure 5d,e), remaining at ≈90% with a variation range of only 1.6%. It should be noted that such a variation range is similar to the error caused by the neural network itself during the training process.

Compared with Von Neumann and near-sensor computing architectures, in-sensor computing architecture has more efficient information processing capabilities. The sensory information could be directly processed by multiple connected sensors, which further eliminates the interface between the sensor and processor and combines the sensing and computing

ADVANCED
SCIENCE NEWS
www.advancedsciencenews.com

ADVANCED
FUNCTIONAL
MATERIALS
www.afm-journal.de

functions.[41] Due to the great reduction of massive information transmission and interaction, power consumption and latency of this architecture will be highly suppressed, and thus it will perform well in time-critical application fields.[67] Here, we proposed a system with an in-sensor computing architecture on the flexible devices to demonstrate motion detection with UV information extraction for the first time, as shown in Figure 5f and Table S1 (Supporting Information). In this real-time application, the scene used for motion detection was a video of a polar bear rolling (Video S1, Supporting Information), in which two device arrays were, respectively, used to perceive images at time t and $t+\Delta t$. It is worth noting that in the visible band, there is almost no difference between the polar bear and the environment, which means that it is very difficult to extract the motion information of the polar bear. Interestingly, the hollow hairs of polar bears allow UV light to pass along the core of the hair and convert it into heat.[68] Therefore, they have a high UV absorption rate, which means that the brightness of a polar bear in the UV light band will be significantly lower than that of the surroundings. Based on this, the strong response of the device to UV light allowed us to conceptually demonstrate the motion detection of a polar bear in snow. After sensing with the device arrays, the UV light signals in the memorized graphs were significantly enhanced, while the visible light signals were almost completely suppressed, which allowed the polar bear's outline to be clearly distinguished from the surroundings (Video S2, Supporting Information). Subsequently, the memorized graphs were passed into a differential amplifier for frame difference calculation. If there was no movement during Δt, the brightness of all pixels in the output image will be close to zero. On the contrary, if there was a moving object, the output image will contain the information of moving object during the two moments. When the Δt is equal to one frame, that is, the step is 1; the result of the motion detection can be seen in Video S3 (Supporting Information). Moreover, by increasing the number of interval frames, we can clearly distinguish the contours of the moving objects in the initial and final images. The conceptual demonstrations of pattern classification, edge enhancement, and motion detection suggest that the proposed flexible device can be used for both static and dynamic recognitions, and thus has great potential for near- and in-sensor computing.

3. Conclusion

In summary, we demonstrated the feasibility of a novel flexible UV neuromorphic sensor based on the VO_2/mica heterostructure. The sensor exhibited not only a reversible photoinduced nonvolatile phase transition feature, but also good flexibility and flexural stability even after 10 000 bending cycles or at a 3 mm bending radius. Furthermore, we constructed an ANN consisting of the proposed devices for static image processing. The recognition rate of the MNIST handwritten database reached 93%, and the variation range under different bending conditions was only 1.6%, demonstrating mechanical stability. The motion detection and recognition functions were successfully realized in UV band through an in-sensor computing architecture, which can greatly reduce the latency due to the massive information interaction. This prototype demonstration of flexible VO_2 UV neuromorphic sensors offers a promising solution for efficient flexible pattern recognition and motion detection systems, and lays the foundation of flexible electronics with neuromorphic functions and superior flexibility.

4. Experimental Section

Sample Preparation: The VO_2 ($\approx$20 and 100 nm) thin films were grown on a (001) mica substrate using an XeCl excimer pulsed laser deposition at a wavelength of 308 nm, a repetition rate of 3 Hz, and an energy density of about 1 J cm^{-2} The VO_2/mica films were conducted in a flowing oxygen atmosphere at 580 °C under a pressure of 1.0 Pa and were cooled down to room temperature at a rate of 20 °C min^{-1}. The deposition rate of VO_2 film was calibrated using X-ray reflection.

Device Fabrication: The VO_2 thin films were patterned into channels with coplanar gate structure by standard lithography and Ar-ion beam etching. The effective device area is 50 μm × 180 μm. Pt electrodes with a thickness of 90 nm were deposited on VO_2/mica films by radio frequency (RF) magnetron sputtering. This was carried out with an RF power of 100 W, a flow rate of 100 sccm Ar, and a working pressure of 5 mTorr. The distance between the gate electrode and the channel was 10 μm. The ionic liquid was used as the dielectric layer for the transistor. By dropping an ionic liquid *N,N*-diethyl-*N*-(2-methoxyethyl)-*N*-methylammoniumbis-(trifluoromethylsulphonyl)-imide (DEME-TFSI) on the channel and gate electrodes, the transistor device was completed.

Material Characterization: The XRD pattern of the VO_2/mica film was measured by using a Rigaku Smartlab instrument with a 2θ range from 20° to 90°, and a step of 0.05°. XAS was performed using the total electron yield method at a background vacuum of 6 × 10^{-7} Torr. Raman spectra were analyzed by using an alpha300 R microscope under 532 nm laser excitation.

Device Measurement: All electrical characteristics were measured in vacuum at room temperature with a Keithley 4200 semiconductor parameter analyzer at a Lakeshore probe station, with the source drain voltage being fixed at 50 mV. The optoelectronic measurements were carried out using an ultraviolet laser with a wavelength of 375 nm. During this experiment, continuous laser equipped with a mechanical shutter was utilized to achieve UV optical pulses.

Supporting Information

Supporting Information is available from the Wiley Online Library or from the author.

Conflict of Interest

The authors declare no conflict of interest.

Author Contributions

G.L., D.X., Z.Z., and Q.Z. contributed equally to this work. C.G. initiated the research. C.G. and K.J. supervised the project. The sample preparation, device fabrication, and device measurement were done by

**ADVANCED
SCIENCE NEWS**

www.advancedsciencenews.com

**ADVANCED
FUNCTIONAL
MATERIALS**

www.afm-journal.de

[1] E. O. Polat, G. Mercier, I. Nikitskiy, E. Puma, T. Galan, S. Gupta, M. Montagut, J. J. Piqueras, M. Bouwens, T. Durduran, G. Konstantatos, S. Goossens, F. Koppens, *Sci. Adv.* **2019**, *5*, eaaw7846.

[2] J. Jiang, Y. Bitla, C.-W. Huang, T. H. Do, H.-J. Liu, Y.-H. Hsieh, C.-H. Ma, C.-Y. Jang, Y.-H. Lai, P.-W. Chiu, W.-W. Wu, Y.-C. Chen, Y.-C. Zhou, Y.-H. Chu, *Sci. Adv.* **2017**, *3*, e1700121.

[3] S.-T. Han, Y. Zhou, V. A. L. Roy, *Adv. Mater.* **2013**, *25*, 5425.

[4] D.-H. Kim, N. Lu, R. Ma, Y.-S. Kim, R.-H. Kim, S. Wang, J. Wu, S. M. Won, H. Tao, A. Islam, K. J. Yu, T.-I. Kim, R. Chowdhury, M. Ying, L. Xu, M. Li, H.-J. Chung, H. Keum, M. Mccormick, P. Liu, Y.-W. Zhang, F. G. Omenetto, Y. Huang, T. Coleman, J. A. Rogers, *Science* **2011**, *333*, 838.

[5] D. Zhang, T. Huang, L. Duan, *Adv. Mater.* **2020**, *32*, 1902391.

[6] L. Lu, C. Jiang, G. Hu, J. Liu, B. Yang, *Adv. Mater.* **2021**, *33*, 2100218.

[7] Q. Shi, Z. Zhang, T. Chen, C. Lee, *Nano Energy* **2019**, *62*, 355.

[8] S. Ham, M. Kang, S. Jang, J. Jang, S. Choi, T.-W. Kim, G. Wang, *Sci. Adv.* **2020**, *6*, eaba1178.

[9] N. Wen, L. Zhang, D. Jiang, Z. Wu, B. Li, C. Sun, Z. Guo, *J. Mater. Chem. A* **2020**, *8*, 25499.

[10] S. Oh, J.-I. Cho, B. H. Lee, S. Seo, J.-H. Lee, H. Choo, K. Heo, S. Y. Lee, J.-H. Park, *Sci. Adv.* **2021**, *7*, eabg9450.

[11] D. H. Kim, H. E. Lee, B. K. You, S. B. Cho, R. Mishra, I.-S. Kang, K. J. Lee, *Adv. Funct. Mater.* **2018**, *29*, 1806338.

[12] Y. Van De Burgt, E. Lubberman, E. J. Fuller, S. T. Keene, G. C. Faria, S. Agarwal, M. J. Marinella, A. A. Talin, A. Salleo, *Nat. Mater.* **2017**, *16*, 414.

[13] H. Wang, Q. Zhao, Z. Ni, Q. Li, H. Liu, Y. Yang, L. Wang, Y. Ran, Y. Guo, W. Hu, Y. Liu, *Adv. Mater.* **2018**, *30*, 1803961.

[14] C.-Q. Chen, D.-M. Ke, T.-T. Zheng, G.-J. He, X.-W. Cao, X. Liao, *Ind. Eng. Chem. Res.* **2016**, *55*, 597.

[15] H. Sun, W. Tian, F. Cao, J. Xiong, L. Li, *Adv. Mater.* **2018**, *30*, 1706986.

[16] X. Hu, X. Zhang, L. Liang, J. Bao, S. Li, W. Yang, Y. Xie, *Adv. Funct. Mater.* **2014**, *24*, 7373.

[17] M. E. Lee, A. M. Armani, *ACS Sens.* **2016**, *1*, 1251.

[18] P. B. Conn, V. I. Chernook, E. E. Moreland, I. S. Trukhanova, E. V. Regehr, A. N. Vasiliev, R. R. Wilson, S. E. Belikov, P. L. Boveng, *PLoS One* **2021**, *16*, e0251130.

[19] L. Yang, W.-L. Tsai, C.-S. Li, B.-W. Hsu, C.-Y. Chen, C.-I. Wu, H.-W. Lin, *ACS Appl. Mater. Interfaces* **2019**, *11*, 47054.

[20] C. J. Wan, Y. H. Liu, P. Feng, W. Wang, L. Q. Zhu, Z. P. Liu, Y. Shi, Q. Wan, *Adv. Mater.* **2016**, *28*, 5878.

[21] Y. Wang, W. Huang, Z. Zhang, L. Fan, Q. Huang, J. Wang, Y. Zhang, M. Zhang, *Nanoscale* **2021**, *13*, 11360.

[22] X. Deng, S.-Q. Wang, Y.-X. Liu, N. Zhong, Y.-H. He, H. Peng, P.-H. Xiang, C.-G. Duan, *Adv. Funct. Mater.* **2021**, *31*, 2101099.

[23] Y. He, H. Dong, Q. Meng, L. Jiang, W. Shao, L. He, W. Hu, *Adv. Mater.* **2011**, *23*, 5502.

[24] Y. Chen, L. Fan, Q. Fang, W. Xu, S. Chen, G. Zan, H. Ren, L. Song, C. Zou, *Nano Energy* **2017**, *31*, 144.

[25] J. Jeong, N. Aetukuri, T. Graf, T. D. Schladt, M. G. Samant, S. S. P. Parkin, *Science* **2013**, *339*, 1402.

[26] M. Nakano, K. Shibuya, D. Okuyama, T. Hatano, S. Ono, M. Kawasaki, Y. Iwasa, Y. Tokura, *Nature* **2012**, *487*, 459.

[27] T. Yajima, T. Nishimura, A. Toriumi, *Nat. Commun.* **2015**, *6*, 10104.

[28] T. Yajima, T. Nishimura, T. Tanaka, K. Uchida, A. Toriumi, *Adv. Electron. Mater.* **2020**, *6*, 1901356.

[29] A. I. Khan, A. Daus, R. Islam, K. M. Neilson, H. R. Lee, H.-S. P Wong, E. Pop, *Science* **2021**, *373*, 1243.

[30] B. H. Mun, B. K. You, S. R. Yang, H. G. Yoo, J. M. Kim, W. I. Park, Y. Yin, M. Byun, Y. S. Jung, K. J. Lee, *ACS Nano* **2015**, *9*, 4120.

[31] N. Bahlawane, D. Lenoble, *Chem. Vap. Deposition* **2014**, *20*, 299.

[32] Y.-B. Kang, *J. Eur. Ceram. Soc.* **2012**, *32*, 3187.

[33] X. Deng, Y.-F. Zhao, N. Zhong, F.-Y. Yue, R. Huang, H. Peng, X.-D. Tang, P.-H. Xiang, Y.-H. Chu, C.-G. Duan, *Adv. Electron. Mater.* **2019**, *6*, 1900742.

[34] C.-I. Li, J.-C. Lin, H.-J. Liu, M.-W. Chu, H.-W. Chen, C.-H. Ma, C.-Y. Tsai, H.-W. Huang, H.-J. Lin, H.-L. Liu, P.-W. Chiu, Y.-H. Chu, *Chem. Mater.* **2016**, *28*, 3914.

[35] H.-T. Zhang, L. Guo, G. Stone, L. Zhang, Y.-X. Zheng, E. Freeman, D. W. Keefer, S. Chaudhuri, H. Paik, J. A. Moyer, M. Barth, D. G. Schlom, J. V. Badding, S. Datta, V. Gopalan, R. Engel-Herbert, *Adv. Funct. Mater.* **2016**, *26*, 6612.

[36] K. A. Hallman, K. J. Miller, A. Baydin, S. M. Weiss, R. F. Haglund, *Adv. Opt. Mater.* **2020**, *9*, 2001721.

[37] S. Lysenko, A. J. Rua, V. Vikhnin, J. Jimenez, F. Fernandez, H. Liu, *Appl. Surf. Sci.* **2006**, *252*, 5512.

[38] S. A. Dönges, O. Khatib, B. T. O'callahan, J. M. Atkin, J. H. Park, D. Cobden, M. B. Raschke, *Nano Lett.* **2016**, *16*, 3029.

[39] Y.-X. Hou, Y. Li, Z.-C. Zhang, J.-Q. Li, D.-H. Qi, X.-D. Chen, J.-J. Wang, B.-W. Yao, M.-X. Yu, T.-B. Lu, J. Zhang, *ACS Nano* **2021**, *15*, 1497.

[40] Y. Chai, *Nature* **2020**, *579*, 32.

[41] F. Zhou, Y. Chai, *Nat. Electron.* **2020**, *3*, 664.

[42] S. Chen, Z. Lou, D. Chen, G. Shen, *Adv. Mater.* **2018**, *30*, 1705400.

[43] H. Wei, Y. Ni, L. Sun, H. Yu, J. Gong, Y. Du, M. Ma, H. Han, W. Xu, *Nano Energy* **2021**, *81*, 105648.

[44] L. Yang, M. Singh, S.-W. Shen, K.-Y Chih, S.-W. Liu, C.-I. Wu, C.-W. Chu, H.-W. Lin, *Adv. Funct. Mater.* **2020**, *31*, 2008259.

[45] F. Sun, Q. Lu, L. Liu, L. Li, Y. Wang, M. Hao, Z. Cao, Z. Wang, S. Wang, T. Li, T. Zhang, *Adv. Mater. Technol.* **2019**, *5*, 1900888.

[46] T.-Y. Wang, J.-L. Meng, Z.-Y. He, L. Chen, H. Zhu, Q.-Q. Sun, S.-J. Ding, P. Zhou, D. W. Zhang, *Adv. Sci.* **2020**, *7*, 1903480.

[47] W. Liang, Y. Jiang, J. Guo, N. Li, W. Qiu, H. Yang, Y. Ji, S.-N. Luo, *Adv. Opt. Mater.* **2019**, *7*, 1900647.

[48] Y. G. Liang, S. Lee, H. S. Yu, H. R. Zhang, Y. J. Liang, P. Y. Zavalij, X. Chen, R. D. James, L. A. Bendersky, A. V. Davydov, X. H. Zhang, I. Takeuchi, *Nat. Commun.* **2020**, *11*, 3539.

[49] D. Lee, D. Yang, H. Kim, J. Kim, S. Song, K. S. Choi, J.-S. Bae, J. Lee, J. Lee, Y. Lee, J. Yan, J. Kim, S. Park, *J. Phys. Chem. C* **2020**, *124*, 17282.

[50] A. C. Jones, S. Berweger, J. Wei, D. Cobden, M. B. Raschke, *Nano Lett.* **2010**, *10*, 1574.

[51] H.-W. Chen, C.-I. Li, C.-H. Ma, Y.-H. Chu, H.-L. Liu, *Phys. Chem. Chem. Phys.* **2021**, *23*, 8908.

[52] X.-B. Chen, *J. Korean Phys. Soc.* **2011**, *58*, 100.

[53] M. Pan, J. Liu, H. Zhong, S. Wang, Z.-F. Li, X. Chen, W. Lu, *J. Cryst. Growth* **2004**, *268*, 178.

[54] S. Zhang, I. S. Kim, L. J. Lauhon, *Nano Lett.* **2011**, *11*, 1443.

[55] M. Kumar, S. Rani, J. P. Singh, K. H. Chae, Y. Kim, J. Park, H. H. Lee, *Appl. Surf. Sci.* **2020**, *529*, 147093.

[56] T. A. Mellan, R. Grau-Crespo, *J. Chem. Phys.* **2012**, *137*, 154706.

[57] K. Appavoo, D. Y. Lei, Y. Sonnefraud, B. Wang, S. T. Pantelides, S. A. Maier, R. F. Haglund, *Nano Lett.* **2012**, *12*, 780.

[58] C. Oh, M. Jo, J. Son, *ACS Appl. Mater. Interfaces* **2019**, *11*, 15733.

[59] A. J. Tan, M. Huang, C. O. Avci, F. Büttner, M. Mann, W. Hu, C. Mazzoli, S. Wilkins, H. L. Tuller, G. S. D. Beach, *Nat. Mater.* **2019**, *18*, 35.

[60] C. Lee, K. G. Rajput, W. Choi, M. Kwak, R. D. Nikam, S. Kim, H. Hwang, *IEEE Electron Device Lett.* **2020**, *41*, 1500.

[61] C. Ge, G. Li, Q.-L. Zhou, J.-Y. Du, E.-J. Guo, M. He, C. Wang, G.-Z. Yang, K.-J. Jin, *Nano Energy* **2020**, *67*, 104268.

[62] H.-Y. Huang, C. Ge, Q.-H. Zhang, C.-X. Liu, J.-Y. Du, J.-K. Li, C. Wang, L. Gu, G.-Z. Yang, K.-J. Jin, *Adv. Funct. Mater.* **2019**, *29*, 1902702.

[63] C. Leighton, *Nat. Mater.* **2019**, *18*, 13.

[64] Y. Ren, J.-Q. Yang, L. Zhou, J.-Y. Mao, S.-R. Zhang, Y. Zhou, S.-T. Han, *Adv. Funct. Mater.* **2018**, *28*, 1805599.

[65] Y. LeCun, C. Cortes, C. J. C. Burges, The MNIST database of handwritten digits, http://yann.lecun.com/exdb/mnist/ (accessed: December 2020).

[66] Y. Lecun, L. Bottou, Y. Bengio, P. Haffner, *Proc. IEEE* **1998**, *86*, 2278.

[67] Z. Zhang, S. Wang, C. Liu, R. Xie, W. Hu, P. Zhou, *Nat. Nanotechnol.* **2021**, *17*, 27.

[68] A. Du, H. Wang, B. Zhou, C. Zhang, X. Wu, Y. Ge, T. Niu, X. Ji, T. Zhang, Z. Zhang, G. Wu, J. Shen, *Chem. Mater.* **2018**, *30*, 6849.